Seeing more with less: human-like representations in vision models

Andrey Gizdov[1,2]   Shimon Ullman[1,3]   Daniel Harari[1,3]

[1]Weizmann Institute of Science
[2]Harvard University
[3]Massachusetts Institute of Technology

{andrey.gizdov, shimon.ullman, hararid}@weizmann.ac.il
https://seeingmorewithless.github.io/

Abstract

Large multimodal models (LMMs) typically process visual inputs with uniform resolution across the entire field of view, leading to inefficiencies when non-critical image regions are processed as precisely as key areas. Inspired by the human visual system's foveated approach, we apply a sampling method to leading architectures such as MDETR, BLIP2, InstructBLIP, LLaVA, and ViLT, and evaluate their performance with variable (foveated) resolution inputs. Results show that foveated sampling boosts accuracy in visual tasks like question answering and object detection under tight pixel budgets, improving performance by up to 2.7% on the GQA dataset, 2.1% on SEED-Bench, and 2.0% on VQAv2 compared to uniform sampling. Furthermore, we show that indiscriminate resolution increases yield diminishing returns, with models achieving up to 80% of their full capability using just 3% of the pixels, even on complex tasks. Foveated sampling prompts more human-like processing within models, such as neuronal selectivity and globally acting self-attention in vision transformers. This paper provides a foundational analysis of foveated sampling's impact on existing models, suggesting that more efficient architectural adaptations, mimicking human visual processing, are a promising research venue for the community. Potential applications of our findings center low power minimal bandwidth devices (such as UAVs and edge devices), where compact and efficient vision is critical.

1. Introduction

The human visual system excels at processing complex visual scenes by efficiently allocating computational resources—a high-resolution focus at the center of gaze (the fovea) and progressively lower resolution toward the periphery [26, 34, 40]. This variable resolution sampling, known as *foveation*, allows humans to perceive fine details where needed while maintaining an awareness of the broader context. This efficient representation enables perception with a limited number of photoreceptors, and a limited diameter of the optic nerve (carrying information from the retina to the brain), balancing detail and field of view (FOV).

In contrast, current large multimodal models (LMMs) in artificial intelligence typically process visual inputs at a uniform resolution across the entire FOV. This approach can lead to inefficiencies, as models may allocate equal computational resources to regions of the image that are less critical for the task at hand. Recent methods, like dynamic tokenization and token merging, aim to alleviate such issues [5, 33]. These techniques embed the full image at the first network layer, and then progressively prune/combine tokens to reduce the computational load in areas of the image that require less precision. However, such methods still embed a *full-resolution* image input to begin with, which becomes a major constraint in portable systems that cannot do computations on-board and instead send images over a narrow communication channel. For small edge devices and UAVs that utilize LPWANs (Low-Power Wide-Area Networks) the bandwidth is small enough, e.g. 70 kbit/s [10, 36], that transmitting full-resolution images of a wide FOV (typically in size much larger than 70kbit) becomes impractical for real-time visual capabilities. To the best of our knowledge, there is no solution addressing the challenge of computationally efficient vision over a narrow communication channel.

Given the efficiency of the human visual system, a natural question arises: *Can we improve the performance and efficiency of LMMs by adopting a foveated sampling scheme similar to that of human vision?*
In this paper, we present the first study that examines the internal representations and performance of existing LMMs when provided with human-like variable resolution images. By applying a biologically inspired
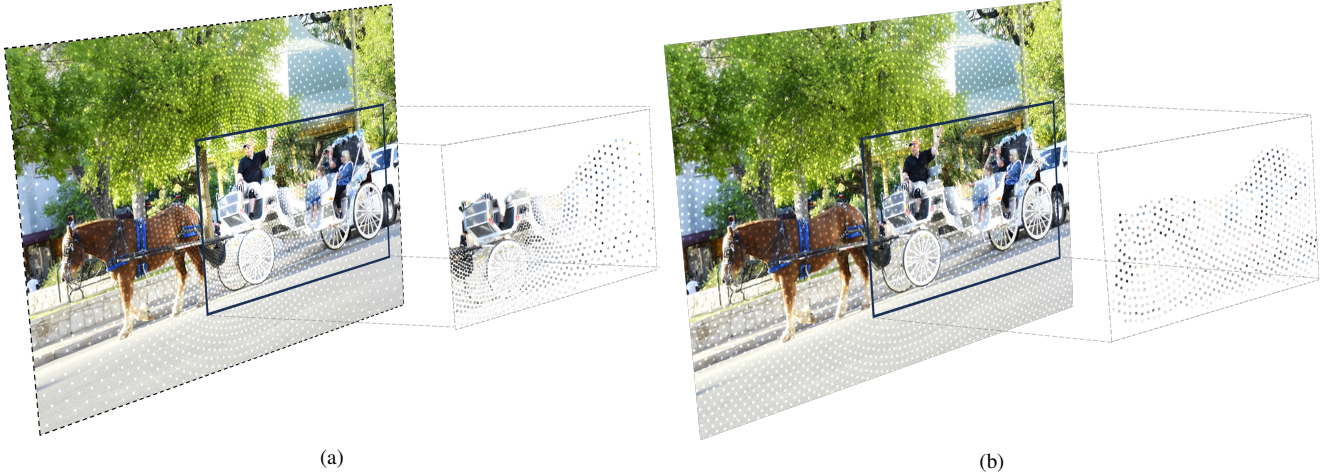
Figure 1. **Alternative sampling schemes. (a) Variable resolution** with peak sample density at the center of fixation and linearly decreasing number of samples with eccentricity. **(b) Uniform resolution** with a constant density of samples. Both schemes distribute an equal number of samples over the entire field of view (FOV) using log-polar coordinates. In this work, we address the question: which of the two alternative (carriage) representations improves on complex visual tasks with existing DNN architectures, given that both alternatives consist of an equal number of samples?

foveated sampling scheme to state-of-the-art LMM architectures—including MDETR [19], BLIP2 [22], Instruct-BLIP [8], LLaVA [24], and ViLT [20]—we investigate what representational changes emerge. Foveated sampling also reduces effective image size, making it suitable for low bandwidth environments, with less accuracy losses.

Our goal is to understand whether existing LMMs can process visual information in a manner similar to the human visual system and how this affects their performance on complex tasks such as visual question answering (VQA) and object detection under extreme pixel budget constraints. Specifically, we aim to address the following questions:

1. **Is foveation beneficial from an information-theoretic perspective?** Can variable resolution sampling improve model performance when constrained by a limited number of pixels (or bandwidth)? (Section 3)

   Answer: Yes, we demonstrate that variable sampling brings gains of up to **2.7%**, **2.1%**, and **2.0%** in accuracy on the GQA [17], SEED-Bench [21], and VQAv2 [13] datasets, respectively, compared to uniform sampling under the same pixel budget. In object detection, variable sampling brings gains of up to **2.2%** on the COCO dataset for vision-only models.

2. **What are the diminishing returns of increasing image resolution?** How does scaling image resolution affect model performance, and is there a point beyond which additional pixels provide minimal benefit? (Section 4)

   Answer: We find that models achieve up to **80%** of their full-resolution performance using just **3%** of the pixels on complex visual tasks, highlighting the diminishing returns of increased image resolution.

3. **Does foveation induce human-like representations in LMMs?** How does variable sampling affect the internal mechanisms of models, such as attention and feature representation? (Section 5)

   Answer: We discover that variable sampling induces human-like processing strategies within models, such as *neuronal selectivity* in CNNs and more *globally* acting self-attention mechanisms in vision transformers, common in many LMMs.

Importantly, we note that the paper does not make computational efficiency claims by making architectural changes to accommodate foveated images, and *does not* explore multiple fixation points. We aim to keep architectures *as they are*, using a single fixation, and provide the first comprehensive analysis of what performance is possible from a purely information theoretic perspective. This allows us to compare and evaluate against existing baselines, while still offering insight into the learned representations. While this paper does not claim gains in computational efficiency, we advocate that foveated architectures are promising, particularly in minimal bandwidth/computation scenarios. We hope future works will explore the adaptation of LMM architectures to variable-sampling grids, inspired by human vision.

2. Experimental setup

2.1. Model architectures

VQA. We utilize several state-of-the-art vision-language models to evaluate the impact of foveation on complex visual tasks, specifically employing BLIP2 [22], ViLT [20], LLaVa [24], MDETR [19], and InstructBLIP [8].
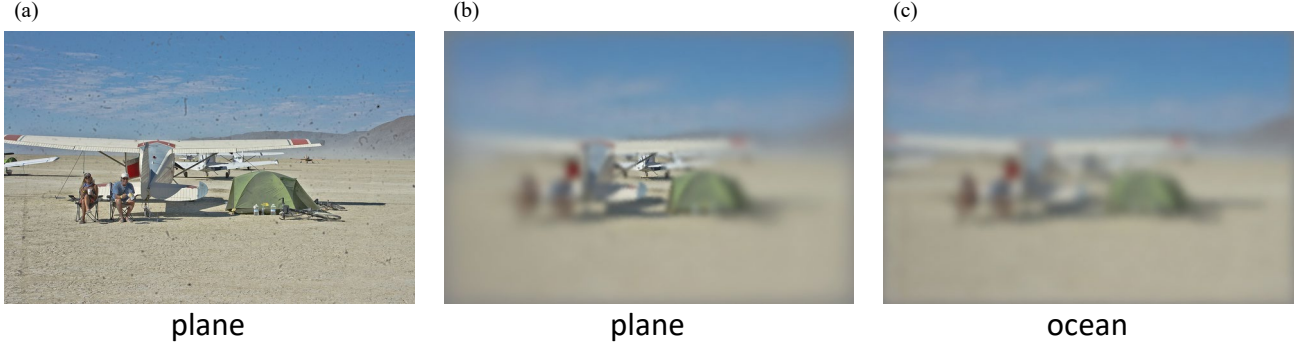
What are the people sitting in front of ?

Figure 2. **Visual question answering example.** ViLT inferenced with three different images, at a 3% sampling budget. **(a)** baseline full resolution, **(b)** variable resolution, **(c)** uniform resolution. The variable model yields the correct answer, as texture and fine-grained details are critical for answering correctly.

Object detection. Most questions in VQA are related to objects, their attributes, relationships and locations. Thus, understanding the representations learned in LMMs requires a foundational understanding of vision-only models under foveation. For this reason, later on in this work we also evaluate the performance of several object detectors with the same sampling schemes. The models we utilize for object detection are the Mask-RCNN [16] and DETR [6].

2.2. Information-matched images

Our first claim is that foveation is beneficial from an information-theoretic perspective. To establish this claim, we introduce the concept of *information-matched* images. These are pairs of images that contain an identical number of samples (pixels) but differ in how these samples are distributed across the image (Figure 1).

Formally, let $I \in \mathbb{R}^{W \times H \times 3}$ be an image from any dataset, where W and H are the width and height of the image, respectively, and 3 corresponds to the RGB color channels. We define a sampling map $S \colon [W] \times [H] \to \{0, 1\}$, where $S(x, y) = 1$ indicates that the pixel at position (x, y) is sampled, and $S(x, y) = 0$ otherwise. The total number of samples is given by $N = \sum_{x=1}^{W} \sum_{y=1}^{H} S(x, y)$.
To create information-matched images, we generate two sampling maps, S_{var} and S_{uni}, corresponding to variable (foveated) and uniform sampling schemes, respectively. These sampling maps can be visualized as dim-white dots overlaid on the original image in Figure 1. They have the same total number of samples N:
$N = \sum_{x=1}^{W} \sum_{y=1}^{H} S_{\text{var}}(x, y) = \sum_{x=1}^{W} \sum_{y=1}^{H} S_{\text{uni}}(x, y)$.
For each sampling map, we extract the sampled pixels from the original image:

$$I_{\text{sampled}}(x, y) = \begin{cases} I(x, y), & \text{if } S(x, y) = 1, \\ 0, & \text{otherwise.} \end{cases} \quad (1)$$

Since the sampled pixels do not cover the entire image, and we aim to *preserve* architectures as they are, we apply an interpolation function to reconstruct the image at the original spatial dimensions. Let $\mathcal{I}$ denote the interpolation operator (e.g., bilinear interpolation). The final image is (Figure 2):

$$\hat{I} = \mathcal{I}(I_{\text{sampled}}). \quad (2)$$

By selecting N s.t. $\frac{N}{W \times H} = 0.03$, for example, we force a 3% sampling density and so on for 10% etc. Ensuring that both sampling schemes use the same number of samples N and images of the same dimensions, we create pairs of images that are *information-matched*. This allows us to *fairly* compare the impact of variable versus uniform sampling on model performance. The specific functions we use, S_{var}, and S_{uni}, are not critical to our results and we refer the reader to the Supplementary "Sampling scheme" section for specific implementation. In this paper, S_{var} follows models of the human visual system by Wilson and Bergen [44] and Poggio et al. [30], S_{uni} picks samples uniformly in a log-polar grid, and S_{baseline}, naturally, picks all pixels in the image.

Fixation point. For technical simplicity we arbitrarily picked the center of the image as the location with highest sample density in S_{var}; as we do not evaluate multiple fixations in our models, picking the middle is intuitively the easiest choice for a single fixation. We dedicate Section 3.2 to demonstrating that the fixation point location is arbitrary and not critical to our claims.

2.3. Training paradigm

VQA. We abstained from training most LMMs due to size constraints. Namely, models BLIP2 [22], ViLT [20], LLaVa [24] and InstructBLIP [8] were *only evaluated* on the datasets discussed bellow using original pretrained

checkpoints. For example, BLIP2 was tested on versions of GQA [17], VQAv2 [13] and SEEDBench [21] that consisted of images with variable sampling (Figure 2b), or uniform sampling (Figure 2c), both never seen during training. Similarly for ViLT, LLaVa and InstructBLIP.

However, since we make claims about *learned* representations, we did fully train the DETR [6] object detection model using a 3% sampling density. This model is used in an LMM, as MDETR [19], and is the entire visual backbone of that LMM. An additional BERT-based transformer for language and the visual embeddings are fused in a transformer encoder-decoder (see Supplementary "Architectures" section for details). We trained DETR from scratch, including the backbone (ResNet101 [15]) which we also pretrained. Our training consisted of pre-processing the necessary datasets (ImageNet, COCO, GQA) with the sampling filters at the 3% density, then training the backbone, then the full DETR model, and then fine-tuning the MDETR on GQA. For hyperparameters, we followed the ResNet101, DETR and MDETR authors, using the hyperparameters in the original papers. As such, we have *three* DETR and MDETR models, one for each input paradigm (baseline, variable at 3%, uniform at 3%).

Object detection. We trained both DETR and MaskR-CNN [16] from scratch, as described in the above paragraph, including their backbones using original parameters.

3. Foveation improves performance

It is clear that providing input images of worse resolution will negatively impact performance, regardless of whether that resolution is distributed in a foveal, i.e. variable, fashion (Figure 1a) or a uniform one (Figure 1b). Having established the concept of *information-matched* images (Section 2.2), we investigate how the distribution of information alone affects performance. We show that a foveal distribution benefits visual tasks more compared to a uniform one.

Uniform sampling as a baseline. We felt it natural to use uniform sampling as a baseline to compare with for two reasons: (1) uniform sampling is the same as downscaling an image in the most trivial sense. This is the most common practice for making images more compact. We think a

Table 1. **Performance on visual question answering using images of 3% sample density.**

Model	Dataset	Uniform	Variable	Full
ViLT [20]	VQAv2 [13]	62.9	**64.9**	81.1
MDETR [19]	GQA [17]	44.1	**46.8**	61.7
BLIP2 [22]	GQA	40.7	**42.3**	44.0
BLIP2	VQAv2	56.2	**57.9**	63.1
InstructBLIP [8]	VQAv2	**66.5**	66.4	73.5
LLaVa-v1.5 [24]	VQAv2	65.1	**65.9**	73.1

comparison here will be most useful to the community. (2) Only uniform sampling allows *fair* comparison with present methods (which use uniform high-resolution images), given that we need to *maintain information-matching*.

3.1. With a 3% sampling density

VQA. We evaluated several pretrained large multimodal models (LMMs) on the VQA task under the three sampling schemes: baseline (full resolution), variable sampling (foveation), and uniform sampling, all at a 3% sampling density (that is $\frac{N}{W \times H} = 0.03$, Section 2.2). Visual question answering (VQA) is a fundamental visual task and requires both the perception of subtle cues and fine details related to object relations, interactions, and causality in a scene.

Using the ViLT model on the VQAv2 dataset, we observed that despite the drastic reduction in pixel count, the model achieved approximately 80% of its full-resolution performance. Specifically, the mean accuracy on the validation split was 81.1% for the baseline, 64.9% for the variable sampling, and 62.9% for the uniform sampling ($M_{var} = 64.9 \pm 19.8\%$, $M_{uni} = 62.9 \pm 19.9\%$). Similarly, the LLaVA model evaluated on the VQAv2 test-dev set achieved a total accuracy of 65.9% with variable sampling, compared to 65.1% with uniform sampling and 73.1% at full resolution. We also tested the MDETR model on the GQA dataset. At a 3% sampling density, the model achieved 46.8% accuracy with variable sampling, outperforming the uniform sampling result of 44.1% ($t[4] = 2.32$, $p = 0.04$). This represents 77% of the full-resolution performance (61.7% accuracy). Table 1 reflects those results.

On BLIP2 [22]. Using the SEEDBench [21] dataset on BLIP2 [22], variable sampling outperformed uniform sampling by 2.1%, achieving 48.6% vs. 46.5% total accuracy ($t[14232] = -6.00$, $p < 1 \times 10^{-6}$), Figure 3. Notably,
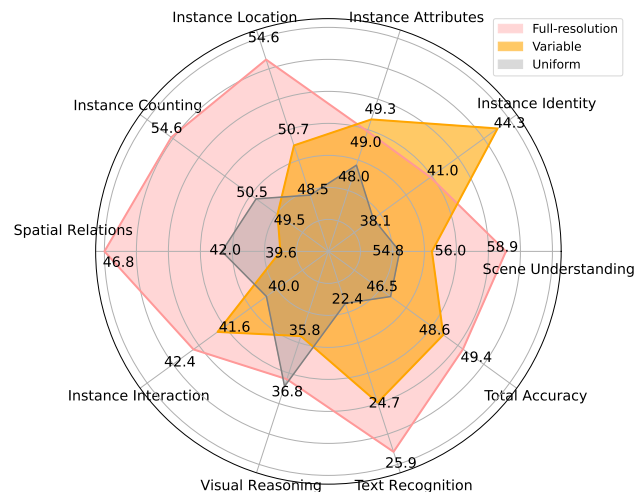

Figure 3. **BLIP2 [22] evaluation on SEED-Bench [21], 3%.**

in some question types such as "Instance Identity," BLIP2 with variable sampling at 3% density even *surpassed* the full-resolution baseline. That is, *BLIP2 using images containing 3% of the information performs better than BLIP2 using images containing 100% of the information*. This result is not a mistake and is also reflected in Figure 5b, where BLIP2 performs better than its baseline on GQA with 30% of samples. We find those results as much exciting as puzzling. They were a surprising finding and, while not the focus of this paper, we hope to explore them in future works. We hypothesize that the selective blur in the variable scheme serves as an "attention direction" mechanism at the input level, which was perhaps not learned sufficiently well during training (hence why the model can benefit from this modality).

3.2. Fixation point bias

Ablation. The datasets under review, GQA, VQAv2, and SEED-Bench, are largely web-scraped and it is natural that they occasionally concentrate on objects positioned at the center of the image, directly aligning with our fixation. At this juncture, the reader might be tempted to accredit the benefits of variable sampling to merely coincide with the pre-existing photographer bias in the datasets. We demonstrate that this is not the case and provide an ablation with fixations positioned close to each corner (see Table 2). The same evaluation is available for other LMMs in the Supplementary "VQA" section. As a secondary control, we also show that the underlying object detection models are *almost* fixation point agnostic (see below).

Object detection. As an additional control for fixation point bias, and as a gateway to explore the results achieved on the complex VQA task, we evaluated the behavior of several models on the underlying task of object detection [23], showing that detection performance is mostly agnostic to fixation point location. For this task, we utilized the DETR (also used for VQA with modulation, as MDETR) and Mask-RCNN architectures on the COCO [23] dataset. COCO is most commonly used for object detection, al-

though it recently saw many uses in large-scale pre-training of LMMs due to its semantic richness (annotations have object location, size, mask, caption etc.). Indeed, all of our LMMs (MDETR, BLIP2, InstructBLIP, LLaVA, ViLT) were trained on COCO in various modalities, which is important for our connection to VQA. In this section, we consider the task of object detection, which, due to being semantically richer than VQA, allows us to measure the degree to which a photographer bias artificially benefits the variable model. The following are two experiments **(1), (2)** that demonstrate a variable model outperforms a uniform one irrespective of fixation location.

Creating annotation bins (1). Consider the COCO validation set $V = I_1, I_2, \ldots, I_{5,000}$, where $I_i \in \mathbb{Z}^{W_i \times H_i \times 3}$ corresponds to the i-th image in the set. There are 5000 images in the COCO validation split, each in RGB format (hence the 3-dimensional domain of I_i). Define a square of size $D \times D$ ($D < W_i$, $D < H_i$ for all i). For instance, D could be 200, since even the smallest images in COCO are larger. Center this square on each validation image, calling the area inside it the high-resolution area (*HRA*). For each ground truth annotation, compute $\frac{P}{A}$, the fraction of its pixel mask area inside the *HRA* (Figure 4a). This metric, the high-resolution inclusion degree (or inclusion degree), measures how much of the annotation is within the *HRA*. The inclusion degree varies with D. For example, an object might have an inclusion degree of 0.5 for a 200×200
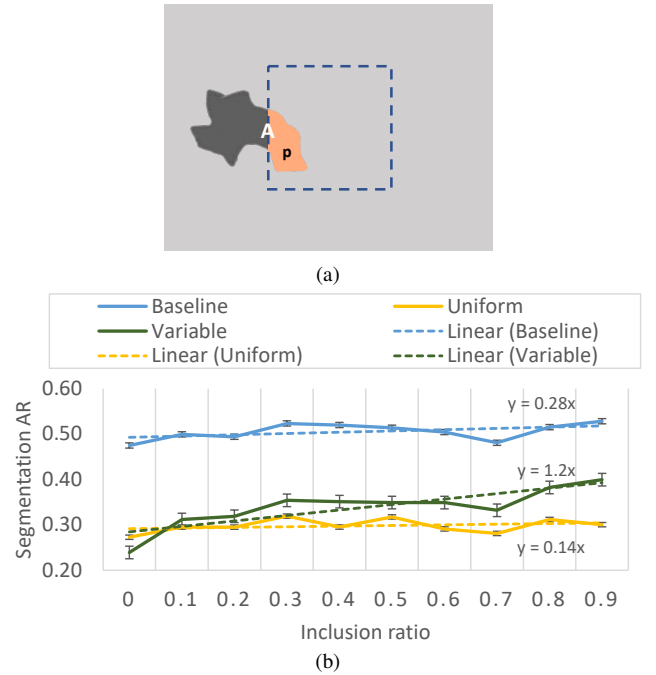

(a)

(b)

Figure 4. **Bin Experiment.** (**a**) High-resolution-area (HRA) = $\frac{P}{A}$. A is the total object area. (**b**) Average Recall (AR, IoU=0.50:0.95) vs HRA.

Table 2. **3% density with corner fixations MDETR [19] on GQA [17]. Uniform** refers to uniform sampling, and **BL**, **BR**, **TL**, and **TR** represent variable sampling with fixations shifted from the center to the bottom-left, bottom-right, etc. directions respectively. Each fixation is 100 pixels away from the center diagonally.

Metric	Uniform	BL	BR	TL	TR
Total	44.1	45.2	45.4	45.0	**45.5**
Attr	57.6	56.1	57.0	56.3	**58.1**
Cat	61.3	**64.6**	64.4	63.2	62.9
Global	93.3	**94.4**	**94.4**	94.0	93.9
Obj	89.9	90.5	**90.7**	90.3	90.7
Rel	34.2	**36.1**	35.9	35.8	36.0

HRA, but 0.3 for a 150×150 *HRA*. We tested *HRA* sizes from 100×100 to 250×250 in 10-pixel increments, with consistent results across sizes.

Annotations are then binned by inclusion degree. The set $G_{0.0-0.1}$ contains annotations with inclusion degrees between 0.0 and 0.1, $G_{0.1-0.2}$ includes those between 0.1 and 0.2, and so on, forming ten bins: $G_{0.0-0.1}$, $G_{0.1-0.2}$, ..., $G_{0.9-1.0}$. Their union covers the entire validation set. Figure 4b shows model Average Recall (AR) across these bins, revealing that variable sampling prevails as soon as 10%-20% of the object area is inside the HRA ($x = 0.1$). Uniform sampling prevails where very little to no part of an object is close to the fixation point ($x = 0$). The conclusion is that, put bluntly, a fixation point placed imperfectly will *almost* always be better than uniformly sampling the image.

Counting samples (2). As an additional control, we constructed an annotation set containing only objects encompassed by an identical sample count, varying only in its distribution pattern: variable or uniform (see Figure 1). The results show a similar performance gap of ∼2.0% in favor of the variable model (See Supplementary "Object detection" section).

4. Diminishing returns of image resolution

We now refer the reader to Figure 5. We interestingly note the pattern of diminishing returns that appears prevalently with the scaling of resolution. The benefit exhibited by the variable sampling at the 3% sampling density (Section 3.1) is evident throughout the entire range of densities. The benefit of variable sampling is larger for lower sampling densities. We attribute this to texture and fine-grained detail. At the 3% density, texture and fine-grained detail are perfectly visible at the center of fixation with variable sampling, while not at all visible in the uniform sampling paradigm. The more we increase the sample density, the more this competitive edge of the variable sampling approach disappears, as the uniform grid begins to capture finer and finer details. We conclude that *texture and fine-grained details are crucial for visual tasks*, as already shown in literature [32, 41].

5. Human-like representations

We now investigate the internal representations of the models to understand the behavior observed in earlier experiments. Specifically, we explore differences in learned representations between the two sampling schemes, focusing on filter kernels, neuronal activations, and their impact on transformer self-attention. (1) Our analysis uses MDETR, which is the only model we trained, but a vision transformer module is common in MDETR, ViLT, BLIP2, InstructBLIP, and LLaVa (granted, in different scales). (2) Aside from this architectural similarity, the aforementioned models all

show a quantitatively similar to MDETR (Figure 5) pattern in performance: all densities show an improvement with variable sampling, and all models converge to a baseline performance at a logarithmic rate. For these two reasons, we consider the representations of the vision transformer in MDETR as sufficiently representative for our discussion of "what happens in vision transformers as a consequence of foveation?".

I. Foveation induces more globally-acting attention in vision transformers. In transformer models like MDETR, self-attention allows each token (representing an image patch) to attend to other tokens, integrating information across the image. We hypothesize that variable sampling encourages the model to attend more globally, effectively combining high-resolution details from the center with contextual information from the periphery.

Formally, we follow [28] and define the *attention distance* d_i for each token i as the average spatial distance to all other

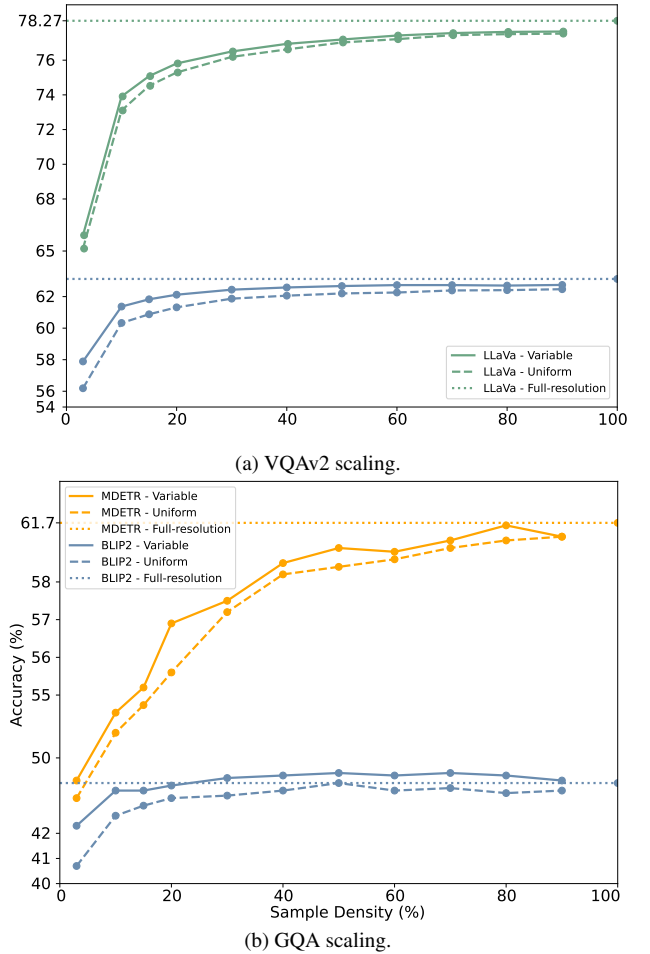(a) VQAv2 scaling.

(b) GQA scaling.

Figure 5. **Evaluation of sample density on models' performance.** Performance of several models on the VQAv2 [13] and GQA [17] datasets.
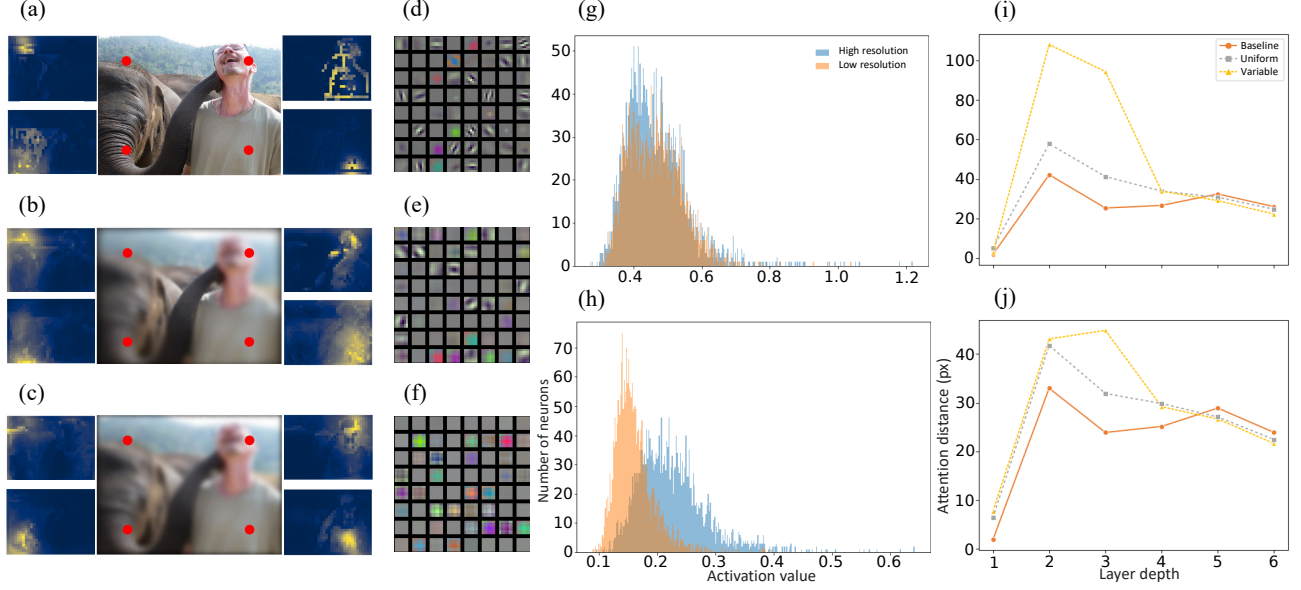
Figure 6. **Interpretability (a, b, c)** Example visualizations of the highest self-attention layer of the DETR transformer model for several tokens located at the periphery. The red dots indicate the tokens' spatial locations. The corresponding attention maps are presented to the left or right of the image (closest to the associated red dot): (a) baseline-full, (b) variable and (c) uniform sampling schemes. **(d, e, f)** Kernel filters of the first convolutional layer for full, variable and uniform resolutions, respectively. **(g, h)** Neuronal activation maps for intermediate layers on high (blue) and low-resolution (orange) crops, showing differences in the feature maps. **(i, j)** Attention distance charts for query tokens located at the central high-resolution area (i) and at the peripheral lower-resolution areas (j), showing large distances in attention spread, see text.

tokens, weighted by the attention weights. Mathematically, let A_{ij} denote the attention weight from token i to token j, and $p_i = (x_i, y_i)$ be the spatial position of token i. Then:

$$d_i = \sum_{j=1}^{N} A_{ij} \cdot \|p_i - p_j\|, \qquad \bar{d} = \frac{1}{N} \sum_{i=1}^{N} d_i. \quad (3)$$

where N is the total number of tokens, and $\|p_i - p_j\|$ is the Euclidean distance between tokens i and j. A larger d_i indicates that token i attends to more distant tokens, implying a more global attention mechanism. The attention distance $\bar{d}$ is averaged across tokens and images for each layer of the transformer's encoder during inference on the COCO validation set using the trained MDETR model.

This computation is performed separately for models trained with variable sampling and uniform sampling. Figure 6(i,j) illustrates how $\bar{d}$ varies across transformer layers. (i) considers only tokens located within the central 10% of the image, coinciding with our fixation point and corresponding to the highest acuity regions, analogous to the densely packed ganglion cells in the human fovea [43]. In contrast, (j) shows the same metric, but for tokens located within the outermost 5% of the image, analogous to the peripheral regions of the human retina, where ganglion cells' density is significantly lower and their receptive fields are much wider, leading to reduced visual acuity and a greater

reliance on broader contextual information [4].

Our results show that models trained with variable sampling exhibit significantly larger $\bar{d}$ across several layers compared to those trained with uniform sampling, as illustrated in Figure 6(i,j), layers 2 and 3. This quantitative measure also aligns with the qualitative visualization of attention maps we see in Figure 6(a,b,c). The red tokens seem to attend more globally in the model trained with variable images (b), compared to the one trained with uniform images (a,c). There is an evident beneficial *information-flow* from the periphery to the center and vice-versa, similar to the human visual cortex [38].

II. Single model generalizes to detect multi-resolution-spanning objects by allowing resolution-specialization in CNNs. The convolutional kernels in CNN-based models are commonly applied uniformly across the entire image. It is therefore not clear if and how CNNs adapt when presented with multiple resolutions within the *same object instance* (as we have in for example Figure 1a). We have demonstrated improved performance of the variable sampling approach, and looking-under-the-hood we now pose the question: what internal adaptations occur in CNN backbone models to facilitate beneficial information-flow from low to high-resolution parts of a single object. We hypothesized that the variable resolution trained models learned a mixed resolution representation, where some neurons

specialize on low-resolutions and other neurons on high-resolutions. Whether this occurs is not a trivial question, since it is entirely possible that the neurons of the network have learned the average resolution in our training set only: producing high dot-products (activations) for mid-resolution occupying object segments and low everywhere else. Formally, our hypothesis becomes:

$$H_0 : \mathbb{P}_0 = \mathbb{P}_1 \quad \text{vs.} \quad H_1 : \mathbb{P}_0 \neq \mathbb{P}_1, \qquad (4)$$

where $\mathbb{P}_0$, $\mathbb{P}_1$ represent the distributions of neuronal activations when the backbone network (ResNet101, variable trained) is inferenced with crops from central (primarily high-resolution) locations, $\mathbb{P}_0$, and crops from peripheral (primarily low-resolution) locations, $\mathbb{P}_1$. Due to $\mathbb{P}_0, \mathbb{P}_1$'s high dimensionality, we employed a classification-based approach, rejecting H_0 at $\alpha = 0.01$ (see Supplementary "Human-like representations" section).

We now refer the reader to Figure 6(g,h). The histograms show the maximal neuronal activation values in several filters from the deep layers of the ResNet101, backbone for our main detection models (MaskRCNN and DETR) and MDETR LMM. We observe that while some filters seem universal (Figure 6g) w.r.t. the resolution of crops, other filters (Figure 6h) exhibit *selectivity*, firing actively from high-resolution crops only. This indeed suggests that the network exhibits neuronal selectivity based on resolution, similar to the human brain [27, 35].

6. Related work

Prior computational work explored the contribution of multiple resolutions to model robustness and improved performance [1, 12]. Some works studied aspects of non-uniform sampling in the visual FOV, including foveal schemes, where samples are distributed densely around a fixation point in the FOV and more sparsely in the periphery [2, 25, 29], but proposing new architectures rather than utilizing existing ones. Early studies, developed models of the human visual system to evaluate the capabilities and limitations of human peripheral vision, but did not address the implications of these models on artificial systems [3, 11]. Followup studies evaluated the impact of these foveated texture-based input representations on artificial vision systems including DNNs, showing that peripheral texture encoding leads to representations with greater generalization, sensitivity to high-spatial frequency and robustness to occlusion [9, 14]. A neuro-computational study suggested that the advantage of peripheral over central vision is due to intrinsic usefulness of features carried by peripheral vision, generating a greater spreading transform in the representational space [42]. The model showed that the two pathways correlate with their neural substrates, LOC and PPA in the brain, but applied to scene classification, the model provides limited insight, as the task can be often performed well at

extremely poor resolutions [39]. Another study suggested that blurry peripheral vision may have evolved to optimize object recognition [31]. Applying DNNs to foveated images around objects of interest, the study showed that DNNs' performance peaked at the human blur decay setting, also benefiting from reduced false detections in the blurry periphery. Other studies investigated the effects of *cortical magnification*, a brain mechanism that allocates more processing units to the densely sampled area of the foveal image [7, 18]. These methods use foveated videos to fit models into embedded systems, achieving a 4× speed-up in frame rate, but showing only a small decrease in recall within the restricted foveal region.

A key limitation of these studies is the absence of a robust comparison with large vision models used on large-scale, complex, datasets such as GQA [17], SEED-Bench [21], and VQAv2 [13]. Furthermore, these studies lack a comparison with prevalent architectures such MDETR [19], BLIP2 [22], InstructBLIP [8], LLaVA [24], and ViLT [20]. Lastly, none of the studies provided a systematic analysis on VQA model performance based on image resolution, nor explored the representations that emerge in *existing* architectures as a consequence of foveation.

7. Conclusions

Growing computational demands are a pain point in the field [37, 46]. We show that efficiency is possible from an information-theoretical perspective. Leading LMMs achieve 80% of their performance with only 3% of the pixels in an image, and almost maximal performance with 50%. We present the case that instead of indiscriminately upscaling images to higher resolutions, the community can benefit from exploring architectural adaptations that utilize a non-uniform, biologically-inspired, image representation.

In VQA, we demonstrate that LMMs benefit from variable sampling on multiple datasets — VQAv2 [13], GQA [17], and SEEDBench [21] — compared to uniform sampling. This is an outstanding finding, mainly from two perspectives. First, by considering the fact that we arbitrarily chose the highest resolution area location of the image (achieving consistent results on central and corner fixations), while the cues required to answer the questions can be anywhere in the scene. Second, the improvement is achieved with a single fixation, without any scanning across the FOV. Humans usually need a few fixations to complete most visual tasks [45], also simpler AI models [2]. Multiple fixations with foveation have potential to drastically improve performance and we hope to explore that in the future. We also reveal human-like, global, self-attention in the transformer, and resolution specialization. The results show the potential of the biologically inspired image representation in future LMM systems, particularly when growing computational demands are a pain point in the field.

Acknowledgements

References

[1] Abdulghani M Abdulghani, Mokhles M Abdulghani, Wilbur L Walters, and Khalid H Abed. Data augmentation with noise and blur to enhance the performance of yolo7 object detection algorithm. In *2023 Congress in Computer Science, Computer Engineering, & Applied Computing (CSCE)*, pages 180–185. IEEE, 2023. 8

[2] Emre Akbas and Miguel P. Eckstein. Object detection through search with a foveated visual system. *PLoS Computational Biology*, 13:1–28, 2017. 8

[3] Benjamin Balas, Lisa Nakano, and Ruth Rosenholtz. A summary-statistic representation in peripheral vision explains visual crowding. *Journal of Vision*, 9(12):13–13, 2009. 8

[4] Jason JS Barton and Michael Benatar. *Field of vision: a manual and atlas of perimetry*. Springer Science & Business Media, 2003. 7

[5] Daniel Bolya, Cheng-Yang Fu, Xiaoliang Dai, Peizhao Zhang, Christoph Feichtenhofer, and Judy Hoffman. Token merging: Your vit but faster. In *The International Conference on Learning Representations*, 2023. 1

[6] Nicolas Carion, Francisco Massa, Gabriel Synnaeve, Nicolas Usunier, Alexander Kirillov, and Sergey Zagoruyko. End-to-end object detection with transformers. In *European conference on computer vision*, pages 213–229, 2020. 3, 4

[7] Danny da Costa, Lukas Kornemann, Rainer Goebel, and Mario Senden. Convolutional neural networks develop major organizational principles of early visual cortex when enhanced with retinal sampling. *Scientific Reports*, 14(1):8980, 2024. 8

[8] Wenliang Dai, Junnan Li, DONGXU LI, Anthony Tiong, Junqi Zhao, Weisheng Wang, Boyang Li, Pascale N Fung, and Steven Hoi. Instructblip: Towards general-purpose vision-language models with instruction tuning. In *Advances in Neural Information Processing Systems*, pages 49250–49267. Curran Associates, Inc., 2023. 2, 3, 4, 8

[9] Arturo Deza and Talia Konkle. Emergent properties of foveated perceptual systems, 2021. 8

[10] Ass Diane, Ousmane Diallo, and El Hadji Malick Ndoye. A systematic and comprehensive review on low power wide area network: characteristics, architecture, applications and research challenges. *Discover Internet of Things*, 5(1):7, 2025. 1

[11] Jeremy Freeman and Eero P Simoncelli. Metamers of the ventral stream. *Nature neuroscience*, 14(9):1195–1201, 2011. 8

[12] Stephanie Fu, Mark Hamilton, Laura E. Brandt, Axel Feldmann, Zhoutong Zhang, and William T. Freeman. Featup:

A model-agnostic framework for features at any resolution. In *The Twelfth International Conference on Learning Representations*, 2024. 8

[13] Yash Goyal, Tejas Khot, Aishwarya Agrawal, Douglas Summers-Stay, Dhruv Batra, and Devi Parikh. Making the V in VQA Matter: Elevating the Role of Image Understanding in Visual Question Answering. *International Journal of Computer Vision*, 127(4):398–414, 2019. 2, 4, 6, 8

[14] Anne Harrington, Vasha DuTell, Mark Hamilton, Ayush Tewari, Simon Stent, William T Freeman, and Ruth Rosenholtz. Coco-periph: bridging the gap between human and machine perception in the periphery. In *The Twelfth International Conference on Learning Representations*, 2023. 8

[15] Kaiming He, X. Zhang, Shaoqing Ren, and Jian Sun. Deep residual learning for image recognition. *2016 IEEE Conference on Computer Vision and Pattern Recognition (CVPR)*, pages 770–778, 2015. 4

[16] Kaiming He, Georgia Gkioxari, Piotr Dollar, and Ross Girshick. Mask R-CNN. *Proceedings of the IEEE International Conference on Computer Vision*, pages 2980–2988, 2017. 3, 4

[17] Drew A Hudson and Christopher D Manning. Gqa: A new dataset for real-world visual reasoning and compositional question answering. In *Proceedings of the IEEE/CVF conference on computer vision and pattern recognition*, pages 6700–6709, 2019. 2, 4, 5, 6, 8

[18] Uziel Jaramillo-Avila and Sean R. Anderson. Foveated Image Processing for Faster Object Detection and Recognition in Embedded Systems Using Deep Convolutional Neural Networks. *Lecture Notes in Computer Science (including subseries Lecture Notes in Artificial Intelligence and Lecture Notes in Bioinformatics)*, pages 193–204, 2019. 8

[19] Aishwarya Kamath, Mannat Singh, Yann LeCun, Gabriel Synnaeve, Ishan Misra, and Nicolas Carion. Mdetr - modulated detection for end-to-end multi-modal understanding. In *Proceedings of the IEEE/CVF International Conference on Computer Vision (ICCV)*, pages 1780–1790, 2021. 2, 4, 5, 8

[20] Wonjae Kim, Bokyung Son, and Ildoo Kim. Vilt: Vision-and-language transformer without convolution or region supervision. In *International Conference on Machine Learning*, pages 5583–5594, 2021. 2, 3, 4, 8

[21] Bohao Li, Rui Wang, Guangzhi Wang, Yuying Ge, Yixiao Ge, and Ying Shan. Seed-bench: Benchmarking multimodal llms with generative comprehension. In *Proceedings of the IEEE Conference on Computer Vision and Pattern Recognition*, 2024. 2, 4, 8

[22] Junnan Li, Dongxu Li, Silvio Savarese, and Steven Hoi. BLIP-2: bootstrapping language-image pre-training with frozen image encoders and large language models. In *ICML*, 2023. 2, 3, 4, 8

[23] Tsung-Yi Lin, Michael Maire, Serge Belongie, James Hays, Pietro Perona, Deva Ramanan, Piotr Dollár, and C Lawrence Zitnick. Microsoft coco: Common objects in context. In *Computer Vision–ECCV 2014: 13th European Conference, Zurich, Switzerland, September 6-12, 2014, Proceedings, Part V 13*, pages 740–755. Springer, 2014. 5

[24] Haotian Liu, Chunyuan Li, Qingyang Wu, and Yong Jae Lee. Visual instruction tuning. In *NeurIPS*, 2023. 2, 3, 4, 8

[25] Hristofor Lukanov, Peter König, and Gordon Pipa. Biologically Inspired Deep Learning Model for Efficient Foveal-Peripheral Vision. *Frontiers in Computational Neuroscience*, 15, 2021. 8

[26] D Marr, T Poggio, and E Hildreth. Smallest channel in early human vision. *Journal of the Optical Society of America*, 70 (7):868–870, 1980. 1

[27] J Anthony Movshon and Peter Lennie. Pattern-selective adaptation in visual cortical neurones. *Nature*, 278(5707): 850–852, 1979. 8

[28] Namuk Park, Wonjae Kim, Byeongho Heo, Taekyung Kim, and Sangdoo Yun. What Do Self-Supervised Vision Transformers Learn? *ICLR*, pages 1–19, 2023. 6

[29] Beatriz Paula and Plinio Moreno. Learning to Search for and Detect Objects in Foveal Images Using Deep Learning. In *Conference on Pattern Recognition and Image Analysis*, pages 223–237. Springer Nature Switzerland, 2023. 8

[30] Tomaso Poggio, Jim Mutch, and Leyla Isik. Computational role of eccentricity dependent cortical magnification. Technical Report CBMM Memo 017, 2014. 3

[31] R. T. Pramod, Harish Katti, and S. P. Arun. Human peripheral blur is optimal for object recognition. *Vision Research*, 200, 2022. 8

[32] Rishi Rajalingham, Elias B Issa, Pouya Bashivan, Kohitij Kar, Kailyn Schmidt, and James J DiCarlo. Large-scale, high-resolution comparison of the core visual object recognition behavior of humans, monkeys, and state-of-the-art deep artificial neural networks. *Journal of Neuroscience*, 38(33): 7255–7269, 2018. 6

[33] Yongming Rao, Wenliang Zhao, Benlin Liu, Jiwen Lu, Jie Zhou, and Cho-Jui Hsieh. Dynamicvit: Efficient vision transformers with dynamic token sparsification. *Advances in neural information processing systems*, 34:13937–13949, 2021. 1

[34] Ruth Rosenholtz. Capabilities and limitations of peripheral vision. *Annual review of vision science*, 2(1):437–457, 2016. 1

[35] Nicole C Rust and James J DiCarlo. Selectivity and tolerance ("invariance") both increase as visual information propagates from cortical area v4 to it. *Journal of Neuroscience*, 30(39): 12978–12995, 2010. 8

[36] Ramon Sanchez-Iborra. Lpwan and embedded machine learning as enablers for the next generation of wearable devices. *Sensors*, 21(15):5218, 2021. 1

[37] Girish Sastry, Lennart Heim, Haydn Belfield, Markus Anderljung, Miles Brundage, Julian Hazell, Cullen O'Keefe, Gillian K. Hadfield, Richard Ngo, Konstantin Pilz, George Gor, Emma Bluemke, Sarah Shoker, Janet Egan, Robert F. Trager, Shahar Avin, Adrian Weller, Yoshua Bengio, and Diane Coyle. Computing power and the governance of artificial intelligence, 2024. 8

[38] Emma EM Stewart, Matteo Valsecchi, and Alexander C Schütz. A review of interactions between peripheral and foveal vision. *Journal of vision*, 20(12):2–2, 2020. 7

[39] Antonio Torralba, Rob Fergus, and William T. Freeman. 80 million tiny images: A large data set for nonparametric object and scene recognition. *IEEE Trans Pattern Anal Mach Intell*, 30:1958–70, 2008. 8

[40] Colwyn B. Trevarthen. Two mechanisms of vision in primates. *Psychologische Forschung*, 31:299–337, 1968. 1

[41] Yoshiaki Tsushima, Kazuteru Komine, Yasuhito Sawahata, and Nobuyuki Hiruma. Higher resolution stimulus facilitates depth perception: Mt+ plays a significant role in monocular depth perception. *Scientific Reports*, 4(1):6687, 2014. 6

[42] Panqu Wang and Garrison W. Cottrell. Central and peripheral vision for scene recognition: A neurocomputational modeling exploration. *Journal of Vision*, 17(4):9–9, 2017. 8

[43] Andrew B Watson. A formula for human retinal ganglion cell receptive field density as a function of visual field location. *Journal of vision*, 14(7):15–15, 2014. 7

[44] Hugh R. Wilson and James R Bergen. A four mechanism model for spatial vision. *Vision Research*, 19(1):19–32, 1979. 3

[45] Jeremy M. Wolfe. Guided search 6.0: An updated model of visual search. *Psychonomic Bulletin & Review*, 28(4):1060–1092, 2021. 8

[46] Carole-Jean Wu, Ramya Raghavendra, Udit Gupta, Bilge Acun, Newsha Ardalani, Kiwan Maeng, Gloria Chang, Fiona Aga, Jinshi Huang, Charles Bai, Michael Gschwind, Anurag Gupta, Myle Ott, Anastasia Melnikov, Salvatore Candido, David Brooks, Geeta Chauhan, Benjamin Lee, Hsien-Hsin Lee, Bugra Akyildiz, Maximilian Balandat, Joe Spisak, Ravi Jain, Mike Rabbat, and Kim Hazelwood. Sustainable ai: Environmental implications, challenges and opportunities. In *Proceedings of Machine Learning and Systems*, pages 795–813, 2022. 8